

# ETHOS – an effective theory of structure formation: predictions for the high-redshift Universe – abundance of galaxies and reionization

Mark R. Lovell<sup>\*1,2,3</sup>, Jesús Zavala<sup>1</sup>, Mark Vogelsberger<sup>4†</sup>, Xuejian Shen<sup>4</sup>, Francis-Yan Cyr-Racine<sup>5</sup>, Christoph Pfrommer<sup>6</sup>, Kris Sigurdson<sup>7</sup>, Michael Boylan-Kolchin<sup>8</sup>, and Annalisa Pillepich<sup>3</sup>

<sup>1</sup>Center for Astrophysics and Cosmology, Science Institute, University of Iceland, Dunhagi 5, 107 Reykjavik, Iceland

<sup>2</sup>Institute for Computational Cosmology, Durham University, South Road, Durham DH1 3LE, UK

<sup>3</sup>Max-Planck-Institut für Astronomie, Königstuhl 17, D-69117 Heidelberg, Germany

<sup>4</sup>Department of Physics, Kavli Institute for Astrophysics and Space Research, Massachusetts Institute of Technology, Cambridge, MA 02139, USA

<sup>5</sup>Department of Physics, Harvard University, Cambridge, MA 02138, USA

<sup>6</sup>Heidelberg Institute for Theoretical Studies, Schloss-Wolfsbrunnengasse 35, 69118 Heidelberg, Germany

<sup>7</sup>Department of Physics and Astronomy, University of British Columbia, Vancouver, British Columbia V6T 1Z1, Canada

<sup>8</sup>Department of Astronomy, The University of Texas at Austin, 2515 Speedway, Stop C1400, Austin, TX 78712-1205, USA

Accepted \*\*\* Received \*\*\*; in original form \*\*\*

## ABSTRACT

We contrast predictions for the high-redshift galaxy population and reionization history between cold dark matter (CDM) and an alternative self-interacting dark matter model based on the recently developed ETHOS framework that alleviates the small-scale CDM challenges within the Local Group. We perform the highest resolution hydrodynamical cosmological simulations (a 36 Mpc<sup>3</sup> volume with gas cell mass of  $\sim 10^5 M_\odot$  and minimum gas softening of  $\sim 180$  pc) within ETHOS to date – plus a CDM counterpart – to quantify the abundance of galaxies at high redshift and their impact on reionization. We find that ETHOS predicts galaxies with higher ultraviolet (UV) luminosities than their CDM counterparts and a faster build-up of the faint end of the UV luminosity function. These effects, however, make the optical depth to reionization less sensitive to the power spectrum cut-off: the ETHOS model differs from the CDM  $\tau$  value by only 10 per cent and is consistent with Planck limits if the effective escape fraction of UV photons is 0.1–0.5. We conclude that current observations of high-redshift luminosity functions cannot differentiate between ETHOS and CDM models, but deep JWST surveys of strongly-lensed, inherently faint galaxies have the potential to test non-CDM models that offer attractive solutions to CDM’s Local Group problems.

**Key words:** cosmology: dark matter – galaxies: high-redshift

## 1 INTRODUCTION

Evidence from the dynamics of gas and stars within galaxies, the large-scale distribution of galaxies and baryonic matter, and the cosmic microwave background has firmly established a paradigm in which gravitational forces in the Universe are dominated by a component that has relatively low thermal velocities at early times (e.g. White et al. 1983; Viel et al. 2013). In addition to being “cold”, this dark matter is generally assumed to be collisionless; this is a central pillar of the dark energy plus cold dark matter ( $\Lambda$ CDM) model that has seen many successes on cosmologically large scales (e.g. Springel et al. 2005; Planck Collaboration et al. 2016a) and is the basis of our current theory for galaxy formation (White & Rees

1978; Blumenthal et al. 1984; see Somerville & Davé 2015 and Naab & Ostriker 2017 for recent reviews). Our ability to simulate the formation and evolution of structure – including galaxies – in this model has increased dramatically, and state-of-the-art simulations are now able to reproduce many properties of the baryonic and total matter distribution over a variety of epochs in cosmologically-representative volumes (e.g., Vogelsberger et al. 2014a; Genel et al. 2014; Dubois et al. 2014; Crain et al. 2015; Schaye et al. 2015).

However, it is important to note that dark matter has only been detected by its gravitational influence, meaning we only have upper limits on its primordial velocity dispersion and collisionality via its effects on baryonic structures and the clustering of matter. Given current constraints, it is certainly possible that dark matter is neither fully cold nor collisionless. An essential question, therefore, is whether dark matter deviates from the phenomenology of a cold and collisionless particle on any scale relevant for astro-

\* email: lovell@hi.is

† Alfred P. Sloan Fellow

physical observations at any cosmological epoch. While many of the most frequently-considered particle candidates for dark matter are indeed cold and collisionless, including weakly-interacting massive particles (WIMPs) and QCD axions (Feng 2010), there are diverse particle physics models in which dark matter has negligible interactions with baryons while having a free-streaming length of  $\sim 10$  kpc, a self-scattering cross section that is comparable to the strength characteristic of the strong nuclear force in the Standard Model of particle physics ( $\sim 10 \text{ cm}^2 \text{ g}^{-1}$ ), or a combination of both.

Such models are also of interest astrophysically, in the context of attempts to understand observations at sub-galactic scales. In this regime, agreement between predictions from CDM models and observations is not established yet as it is on large scales. Even in systems where dark matter dominates the gravitational potential, astrophysical systems are generically less dense and less abundant than naive CDM predictions (see Bullock & Boylan-Kolchin 2017 for a recent review). These potential “small-scale challenges” – the cusp-core, missing satellite/field-dwarf, and too-big-to-fail problems (Flores & Primack 1994; Moore 1994; Moore et al. 1999; Klypin et al. 1999; Zavala et al. 2009; Papastergis et al. 2011; Klypin et al. 2015; Boylan-Kolchin et al. 2011) – have been the astrophysical motivation for considering dark matter models that abandon the cold or collisionless assumptions of standard CDM.

These challenges might however be solved by the complex and not yet fully understood physics of galaxy formation and evolution. In fact, simulations rooted firmly in the CDM paradigm have demonstrated that star formation feedback may be able to alleviate many of the apparent tensions facing the CDM model. In particular, feedback-driven gravitational potential fluctuations can heat dark matter (Pontzen & Governato 2012), reducing central densities and often forming dark matter cores (Governato et al. 2010; Zolotov et al. 2012; Teyssier et al. 2013; Munshi et al. 2013; Di Cintio et al. 2014; Oñorbe et al. 2015; Chan et al. 2015; Tollet et al. 2016; Fitts et al. 2017; Read et al. 2017). Thus, signatures of non-standard dark matter can be difficult to disentangle from those of baryonic feedback. One possibility in the low-redshift Universe is to study the internal kinematics of the least luminous galaxies possible ( $M_\star \lesssim 10^6 M_\odot$ ), as recent results indicate that feedback-induced cores will be minimal or non-existent in such systems (Di Cintio et al. 2014; Tollet et al. 2016; Fitts et al. 2017, though see Sawala et al. 2016b and Read et al. 2017). Firmly establishing definitive tests in the local and distant Universe are therefore of crucial importance for understanding whether or not changes are required to the CDM paradigm.

Observationally, the power spectrum of dark matter is required to extend at least down to the mass scale of dwarf galaxies ( $M_{\text{dm}} \approx 10^{10} M_\odot$ ) without exhibiting a damping signature, with constraints coming from counts of satellite galaxies in the nearby Universe (Polisensky & Ricotti 2011; Lovell et al. 2014; Kennedy et al. 2014; Kim et al. 2017) and structure in the Lyman- $\alpha$  forest at higher redshifts (e.g. Viel et al. 2013; Iršič et al. 2017). Quoted limits at high redshifts are typically sensitive to a number of effects (e.g., uncertainties in the thermal history of the Universe and the production mechanism of dark matter; see, e.g., Puchwein et al. 2012; Bozek et al. 2016; Garzilli et al. 2017; Murgia et al. 2017), but it remains possible that the particle nature of dark matter is important (or dominant) in setting the minimum scale for galaxy formation through damping of primordial perturbations.

Dark matter self-interactions (e.g. Spergel & Steinhardt 2000; Feng et al. 2009; Loeb & Weiner 2011) affect structure in a different manner: as opposed to suppressing structure in the linear

regime, dark matter self-interactions operate in the highly non-linear regime of structure formation, affecting primarily the dense centres of dark matter haloes. Such models have been explored in the context of structure formation simulations for nearly two decades, under the umbrella term of self-interacting dark matter (SIDM; e.g. Yoshida et al. 2000; Davé et al. 2001; Colín et al. 2002). Recent years have seen a new generation of simulations demonstrating SIDM’s viability over the full range of scales relevant for galaxy formation and its ability to mitigate outstanding CDM challenges at the scale of dwarf galaxies via dark matter physics (e.g. Vogelsberger et al. 2012; Rocha et al. 2013; Zavala et al. 2013; Vogelsberger & Zavala 2013; Vegetti & Vogelsberger 2014; Vogelsberger et al. 2014b; Elbert et al. 2015; Dooley et al. 2016; Kaplinghat et al. 2016; Creasey et al. 2017; Kamada et al. 2017; Robles et al. 2017; Brinckmann et al. 2018). For a recent review on SIDM see Tulin & Yu (2018).

The ETHOS framework (Cyr-Racine et al. 2016; Vogelsberger et al. 2016) generalises structure formation theory to allow for non-gravitational interactions – both self-collisions (as in SIDM) and a cut-off in the primordial power spectrum caused by hidden interactions between dark matter and relativistic particles in the early Universe (e.g. Hofmann et al. 2001; Chen et al. 2001; Böhm et al. 2002; Green et al. 2004; Bertschinger 2006; Bringmann & Hofmann 2007; van den Aarssen et al. 2012; Cyr-Racine & Sigurdson 2013). Such cut-offs are different in nature than the free-streaming cut-off in Warm Dark Matter (WDM), but they also result in a suppression of the abundance of galaxies, a helpful feature to explain the observed dearth of dwarf galaxies (see Böhm et al. 2014 and Buckley et al. 2014 for analyses of these models with simulations). In Vogelsberger et al. (2016), using dark-matter-only simulations, a specific benchmark model (ETHOS-4) was found that is consistent with current constraints from the population of Milky Way satellite haloes and is able to reduce both the predicted abundance of satellites and their dark matter densities relative to the predictions from CDM, thereby addressing outstanding small-scale issues of the  $\Lambda$ CDM paradigm in a compelling way.

This benchmark model, which we call ETHOS from this point onwards for simplicity, has been calibrated to match broadly the observed satellite subhalo properties of the Milky Way. Therefore, it has only been explored in the local Universe. In order to fully assess the viability of this model we must however compare its predictions to observables in other environments. One such regime is the high-redshift Universe. The properties of galaxies at high redshift are affected by the collapse time of their host haloes. This process is delayed in dark matter models with primordial power spectrum cut-offs (e.g. for WDM, Colín et al. 2000; Bode et al. 2001; Lovell et al. 2012, 2016). In the ETHOS model, we therefore expect an impact on the high-redshift mass and luminosity functions with potentially detectable differences with respect to the CDM case. Furthermore, a delayed collapse time, coupled to the lower number density of small galaxies, should lead, at least naively, to lower star formation rates, which in turn result in a lower production rate of high-energy, ionizing photons and subsequently to a later epoch of reionization. If the delay in reionization is in severe tension with cosmic microwave background (CMB) estimates (Planck Collaboration et al. 2016b), then the model is ruled out. In the context of WDM, recent studies using semianalytic modelling of the galaxy population have shown that this delay does occur, with the end results being sensitive to assumptions about galaxy formation physics. Particularly for reionization constraints, the role of strong high-redshift starbursts in WDM leads to galaxies that are brighter in the UV than is the case in CDM, therefore partially compensating for the deficit in the

number of galaxies (Bose et al. 2016; Rudakovskiy & Iakubovskiy 2016; Dayal et al. 2017).

In this paper, we confront the benchmark ETHOS model with constraints from the high-redshift Universe. We perform the first high resolution, cosmological, hydrodynamical simulations within the ETHOS framework, taking into account the matter power spectrum cut-off and the self-interactions of dark matter particles, while baryonic physics is incorporated in a state-of-the-art galaxy formation and evolution model. We obtain predictions for the high-redshift luminosity functions and the number density of ionizing photons. We compare these to a CDM simulation with the same initial conditions, phases and treatment of baryonic physics. We then assess our results in the context of current observational constraints to test the viability of the ETHOS model, and present luminosity function predictions for the James Webb Space Telescope (JWST).

This paper is organised as follows. In Section 2 we describe our methods for simulating the high-redshift galaxy population with CDM and ETHOS, while in Section 3 we present our results on the luminosity functions and optical depth for reionization. We present our conclusions in Section 4.

## 2 SIMULATIONS

We perform cosmological hydrodynamical simulations within CDM and ETHOS using the AREPO code (Springel 2010) combined with a well-tested galaxy formation model (Vogelsberger et al. 2013; Torrey et al. 2014; Vogelsberger et al. 2014a,c; Genel et al. 2014; Weinberger et al. 2017; Pillepich et al. 2018). The AREPO code has been significantly extended to include isotropic and elastic self-interactions (Vogelsberger et al. 2016) following arbitrary velocity-dependent interaction cross sections. The ETHOS simulation employs the primordial power spectrum cut-off and self-interaction cross section of the ETHOS-4 model presented in Cyr-Racine et al. (2016) and Vogelsberger et al. (2016)<sup>1</sup>. The cosmological parameters for the simulations are: matter density  $\Omega_0 = 0.302$ , dark energy density  $\Omega_\Lambda = 0.698$ , baryon density  $\Omega_b = 0.046$ , Hubble parameter  $H_0 = 100 h \text{ km s}^{-1} \text{ Mpc}^{-1} = 69.1 \text{ km s}^{-1} \text{ Mpc}^{-1}$ , power spectrum normalisation  $\sigma_8 = 0.838$ , and power spectrum slope index  $n_s = 0.967$ , which are consistent with recent Planck data (Planck Collaboration et al. 2014; Spergel et al. 2015). We perform simulations over a  $(36.2 \text{ Mpc})^3$  periodic volume with a dark matter particle mass of  $1.76 \times 10^6 M_\odot$  and a comoving dark matter softening length of 724 pc. The average gas cell mass is  $2.69 \times 10^5 M_\odot$  and the gas softening length is adaptive with a comoving minimum of 181 pc. These simulations are currently the best resolved uniform box hydrodynamical simulations of alternative dark matter models.

The initial conditions of both simulations, CDM and ETHOS, share the same random field, but the ETHOS initial conditions have a fluctuation spectrum with an amplitude rescaled by the ETHOS linear matter power spectrum (taken from Cyr-Racine et al. 2016). This contains a small-scale primordial cut-off in the power spectrum including dark acoustic oscillations (DAOs) due to the interaction of the dark matter particles with the relativistic species (dark radiation). This cut-off occurs at a wavenumber of  $13 h^{-1} \text{ Mpc}$ , which is remarkably similar to the cut-off wavenumber of the

<sup>1</sup> See Table 1 in Vogelsberger et al. (2016) for the particle physics and effective parameters of the ETHOS-4 model. Fig. 1 on that paper shows the linear power spectrum and the velocity-dependent transfer cross section for this model.

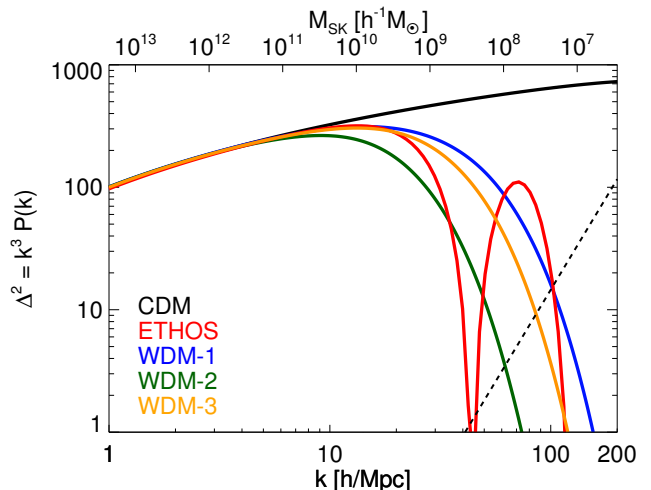


**Figure 1.** Dimensionless linear matter power spectra for CDM and ETHOS, shown as black and red solid lines, respectively. Also included are three warm dark matter models: WDM-1, WDM-2 and WDM-3. These are three sterile neutrino models in which the sterile neutrino mass is 7 keV and the lepton asymmetry is  $L_6 = 8$  (blue),  $L_6 = 11.2$  (green), and  $L_6 = 8.9$  (orange) for WDM-1, WDM-2 and WDM-3 respectively. In the upper  $x$ -axis we show the halo mass scale associated with each wavenumber, using a sharp  $k$ -space cut-off. The dashed line shows the power spectrum due to Poisson noise in our simulations.

7 keV sterile neutrino that could be responsible for the unidentified 3.5 keV emission line in some galaxy clusters and the Andromeda galaxy (Bulbul et al. 2014; Boyarsky et al. 2014). We present the ETHOS power spectrum in Fig. 1, along with power spectra for three 7 keV sterile neutrino models with different free-streaming lengths, as originally presented in Lovell et al. (2016, 2017). These models are characterized by the lepton asymmetry  $L_6$ , defined as  $10^6$  times the difference in lepton and anti-lepton abundance normalised by the entropy density. The  $L_6 = 8$  model has the shortest free-streaming length of any 7 keV sterile neutrino. On the other hand,  $L_6 = 11.2$  has the longest free-streaming length expected from a 7 keV sterile neutrino responsible for the unidentified 3.5 keV emission line in some galaxy clusters and the Andromeda galaxy (Bulbul et al. 2014; Boyarsky et al. 2014). The case with  $L_6 = 8.9$  is in between and peaks at the same wavenumber as the ETHOS benchmark model. Qualitatively, the ETHOS model is similar to the cooler 7 keV sterile neutrino models, including those that match the 3.5 keV line; the main difference being the DAOs in ETHOS, which are not present in WDM models. The detailed parameter calibration leading to the ETHOS benchmark model is described in Vogelsberger et al. (2016).

A well known problem for N-body simulations of models with a resolved cut-off scale in the linear matter power spectrum is the spurious fragmentation of filaments, which is ultimately caused by the power spectrum due to shot noise in a simulation exceeding the small-scale power at wavenumbers higher than the physical cut-off of the model (see dashed line in Fig. 1). The spurious fragments coalesce into haloes that could potentially host galaxies, thus affecting our results. The characteristic mass scale below which these spurious haloes form and dominate the mass function,  $M_{\text{lim}}$ , has been shown by Wang & White (2007) to be well described by  $M_{\text{lim}} = 10.1 \bar{\rho} d k_{\text{peak}}^{-2}$ , where  $\bar{\rho}$  is the mean density of the Universe,  $k_{\text{peak}}$  is the wavenumber at which the dimension-

less matter power spectrum attains its maximum amplitude, and  $d$  is the mean inter-particle separation of the simulation. For the purpose of spurious fragmentation, ETHOS is similar to WDM with an equivalent peak in the dimensionless power spectrum, as the amplitude of first dark acoustic peak is well below that of the main power spectrum peak. For the benchmark model we analyse, we find:  $M_{\text{lim}} \sim 1.2 \times 10^8 M_{\odot}$ , or  $\sim 70$  particles for the resolution of our simulations. We comment below on whether these objects may have any effect on our results.

We note that our simulations do not include radiative transfer and we therefore cannot study reionization in a fully self-consistent framework. In fact, our simulations are set up with a spatially uniform, time-dependent UV background, which is not coupled to local star formation (this is a standard procedure when radiative transfer is not included, and the particular implementation we used is described in Section 2.4 of [Vogelsberger et al. 2013](#)). The simulations presented here follow the gradual build up at high redshifts of the UV background as prescribed by [Faucher-Giguère et al. \(2009\)](#). Our approach is based instead on computing the reionization history *a posteriori* using as input the star formation rate density in our simulations. Our purpose here is to present a first-order approximation of the expected relative differences between the reionization history of CDM and the ETHOS benchmark model. We keep this limitation in mind when interpreting our results and note that all other cosmological hydrodynamical simulations that do not self-consistently model radiative transfer are subject to the same limitation.

### 3 RESULTS

Our goal is to study two high-redshift observables that could be used to distinguish ETHOS models from CDM. The first is the abundance of galaxies at high redshift, which is expected to differ towards lower masses due to the primordial cut-off in the power spectrum. Second, changes in the high-redshift galaxy population will also impact the UV photon budget, thereby changing the details of the reionization history in both models. We note that although the first effect implies the second one, there are various compensating effects that can invalidate the simple argument in favour of an overall reduced UV photon budget in ETHOS at high redshift. We further note that the two effects are mostly caused by the damping in the power spectrum and are not expected to be influenced significantly by dark matter self-interactions, which are mainly responsible for shaping the inner regions of collapsed haloes towards lower redshifts.

We start our exploration of the high-redshift model differences with Fig. 2, where we give a visual impression of our simulations through a series of maps of the intergalactic medium (IGM) that qualitatively show the differences between the two dark matter models. We include maps for the entire simulation volume and also a subregion of the volume that is host to a star-forming overdensity. The large-scale maps are presented at  $z = 11$ , and the zoomed region at both  $z = 11$  and  $z = 6$ .

The large scale structure of filaments, nodes, and voids is identical in the two models, which is not surprising since ETHOS models preserve the large-scale clustering characteristics of CDM. Differences become visible only at the smallest resolvable scales, at which we find in general more structure in CDM than in ETHOS due to the primordial damping of the power spectrum. These differences become more apparent in the zoomed maps and their accompanying difference maps. Here we also find that the heating of gas

by galaxies is different in the two models. The number density of heating sites is lower in the ETHOS model; the small black regions in the difference maps show where a halo has collapsed in CDM but not in ETHOS. Furthermore, the expanding bubbles, driven by stellar feedback, are in general smaller in ETHOS, since they formed later than in CDM and had less time to expand. This phenomenon can be appreciated even better in the difference maps (right panels of Fig. 2): the regions that are hotter in ETHOS (white) are often located within hot shells in CDM (black), thus showing how the feedback bubble generation in ETHOS lags behind that of CDM.

#### 3.1 Abundance of galaxies at high redshift

The primordial power spectrum cut-off impacts the low-mass end of the ETHOS halo-mass/luminosity function. We investigate this effect quantitatively by measuring the abundance of dark matter haloes and the  $U$ -band luminosity function of the galaxies they host at  $z \geq 6$  in both models. We note that ongoing star formation in galaxies is traced more directly with the intrinsic far UV (FUV) luminosities, corresponding approximately to a rest frame wavelength of 150 nm, than by the  $U$ -band we use here, centred at around 365 nm. We study the FUV luminosity function in detail further below when we show predictions for JWST (see section 3.1.3).

We remark that, for simplicity, throughout this work we refer to *intrinsic* luminosities (absolute magnitudes) computed in a given band/wavelength without accounting for dust attenuation. The procedure to compute FUV luminosities from the simulation data is described further below in section 3.1.3. For the other bands/wavelengths used in this work, the procedure is similar. Since we are avoiding the complication of dust modelling, we are also not properly taking into account the observational consequences that dust has in suppressing intrinsic luminosities, in particular the relevance it has in the observed  $U$ -band magnitudes of galaxies. Since this suppression is connected to the star formation history in a given galaxy, it will likely be different in ETHOS than in CDM. As we mention elsewhere, we are deferring the full and more detailed analysis of the properties of the ETHOS galaxies near the cut-off of the power spectrum for a future work.

##### 3.1.1 Impact on the halo mass function

To start, we show the mass function of haloes at redshifts in the range  $z = [12, 6]$  in Fig. 3. We use the radius enclosing 200 times the critical density to define the halo mass,  $M_{200}$ . Both CDM and ETHOS show a strong cut-off at around  $2 - 3 \times 10^7 M_{\odot}$ , which is the resolution limit for the CDM case corresponding to  $\sim 20$  particles. There is also a suppression in the ETHOS halo abundance compared to CDM by up to a factor of several visible at that mass scale. However, these scales are clearly affected by spurious fragmentation: there is a clear upturn in the mass function below  $\sim 10^8 M_{\odot}$ , which agrees with the limiting mass due to discreteness effects mentioned in Section 2. This mass scale can be considered as the effective halo mass resolution for the ETHOS case. The difference in the abundance of haloes at this resolved scale relative to CDM is clearly apparent (a factor of  $\sim 5.5$  at  $z = 6$ ). This would naively suggest that the abundance of galaxies inhabiting these haloes, and thus the production rate of ionizing UV photons, is suppressed in ETHOS relative to CDM by a similar factor. However, a halo can only act as a source of ionizing photons if the gas it accretes can radiatively cool and collapse to form a luminous



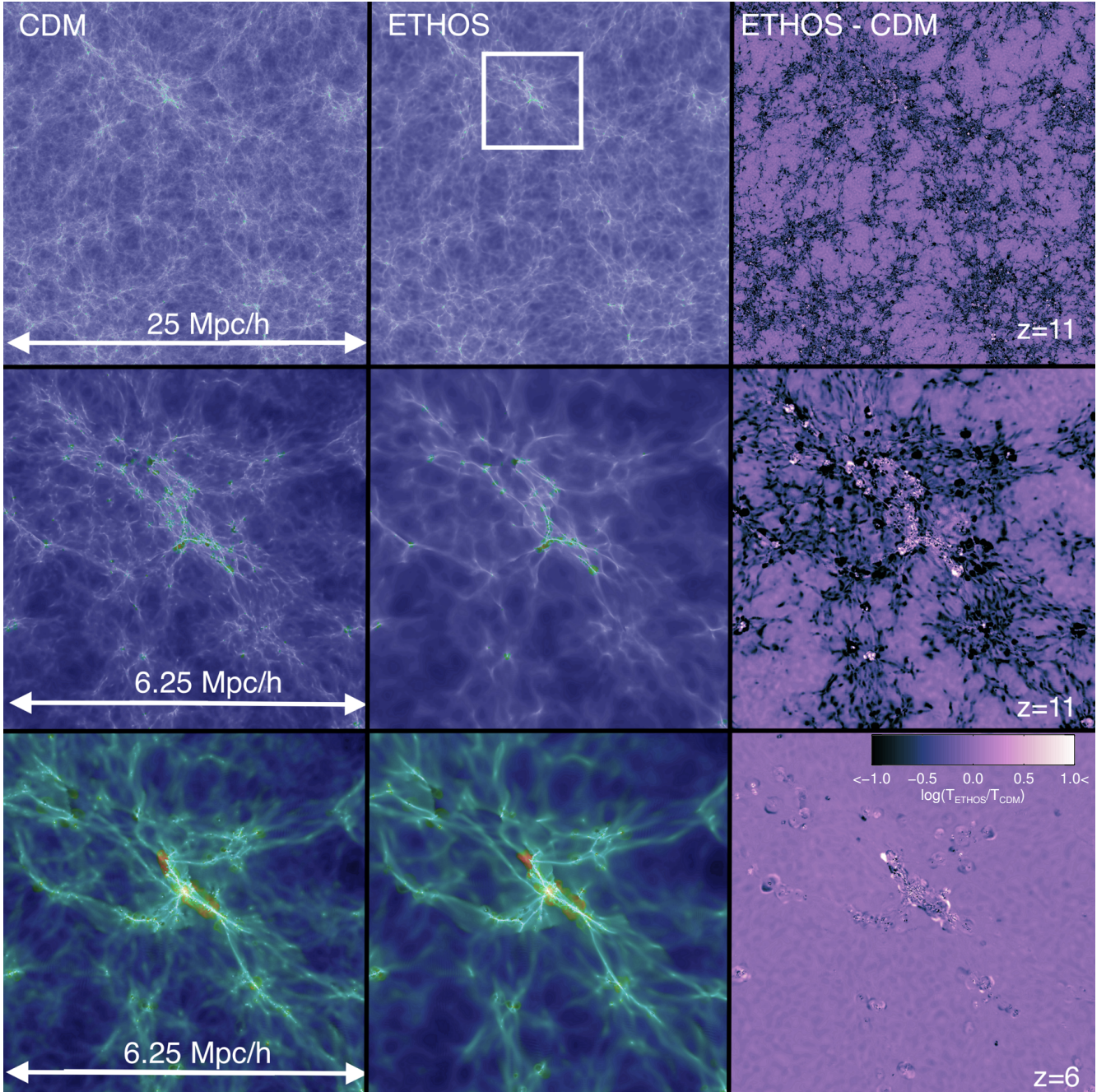


**Figure 2.** Maps of IGM gas temperature in CDM (left panels) and ETHOS (middle panels). The image intensity shows squared gas density (with arbitrary normalisation), and the colour shows the temperature:  $\leq 10^4$  K gas is shown in purple,  $10^5$  K in green and  $\geq 10^6$  K in red. The top panels show the entire box at  $z = 11$ , the middle two panels a zoom-in of the region highlighted with a white box in the top middle panel at the same redshift, and the bottom panels show the same zoomed region at  $z = 6$ . Each image slice is 400 kpc thick; all lengths scales quoted are comoving. In the right-hand panels we show the difference map between the temperature of the CDM and ETHOS maps. Lighter regions are hotter in ETHOS and darker regions are hotter in CDM (colour bar in the bottom right panel).

galaxy. If the proportion of haloes that host galaxies – the so-called luminous fraction – is different between CDM and ETHOS, then this effect will be relevant for the production rate of ionizing photons in galaxies.

We therefore plot, in the top panel of Fig. 4, the ratio of ETHOS and CDM luminous fractions as a function of halo mass, where the luminous fraction is defined as the fraction of haloes that contain a stellar mass larger than  $3 \times 10^6 M_\odot$ . We choose this stel-

lar mass threshold to avoid spurious effects due to limited resolution, and also restrict our plot to haloes of mass  $M_{200} \geq 10^9 M_\odot$  as the galaxies hosted in  $M_{200} < 10^9 M_\odot$  haloes rarely meet the stellar mass threshold, and are therefore subject to shot noise; note that we therefore resolve the haloes of all galaxies with this stellar mass. The plot demonstrates that below the halo mass where the halo mass function in ETHOS starts to deviate from CDM, the luminous fraction is actually higher in ETHOS than in CDM. The

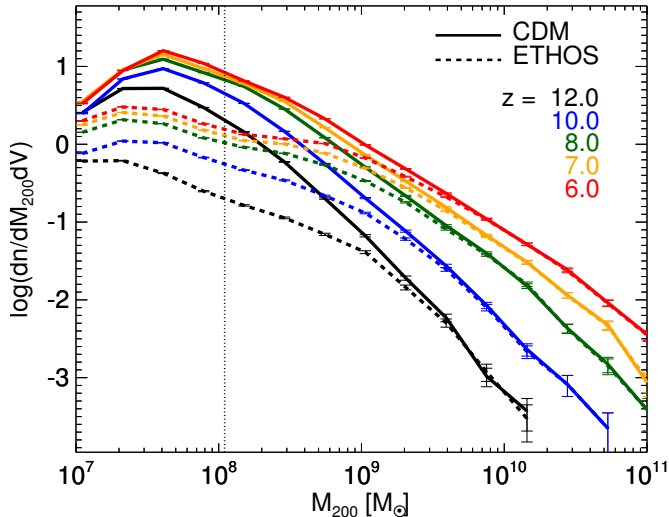


**Figure 3.** Halo mass functions for CDM (solid lines) and ETHOS (dashed lines) at five redshifts:  $z=[12,10,8,7,6]$  shown in black, blue, green, yellow and red respectively. The error bars are Poissonian. The vertical dotted line is the effective halo mass resolution we use for both models, corresponding to the appearance of spurious haloes in ETHOS.

difference grows towards lower masses and becomes substantial below the halo resolution limit, although the statistics of haloes hosting galaxies with stellar mass beyond the chosen threshold are poor in this limit. We have found that lowering the stellar mass threshold eases the difference between the two models somewhat, which emphasizes the fact that although  $< 10^{10} M_{\odot}$  CDM haloes do host galaxies, they are less massive than their ETHOS counterparts. This plot indicates that despite their lower number, ETHOS haloes with scales near the primordial cut-off in the power spectrum have a higher star formation efficiency than their CDM counterparts. We speculate that this higher efficiency is the result of an enhancement in starbursts, as the first haloes in ETHOS form through a monolithic collapse and not hierarchically. As these gas-rich haloes merge, they produce brighter starbursts than in the CDM case. A similar phenomenon has been described in the WDM context (Bose et al. 2016, 2017), as we discuss below.

There might be an environmental effect as well linked to this phenomenon. In ETHOS, galaxies within haloes of masses between  $(10^8 - 2 \times 10^9) M_{\odot}$  are the first to form, with no prior star formation in less massive haloes. Thus, although there is a dearth of haloes in this mass range, caused by the primordial power spectrum cut-off, there is also a compensating effect since the absent haloes in ETHOS are clearly not a source of (stellar) feedback into the local environment around them, as they are in the CDM case. Visually, this can be appreciated in the right panels of Fig. 2 by the absence in ETHOS of the galactic wind bubbles driven by stellar feedback within the smallest haloes seen in CDM. Thus, we speculate that star formation within these smallest haloes is an additional source of heating (through stellar feedback) of the local environment, which might suppress star formation within nearby larger haloes. These same haloes would be unaffected in ETHOS, where this source of heating is absent. Fig. 2 provides a degree of qualitative evidence for this speculative mechanism, since the extent and density of feedback-driven bubbles is seemingly larger in the CDM case (bottom-right panel of Fig. 2). That these bubbles

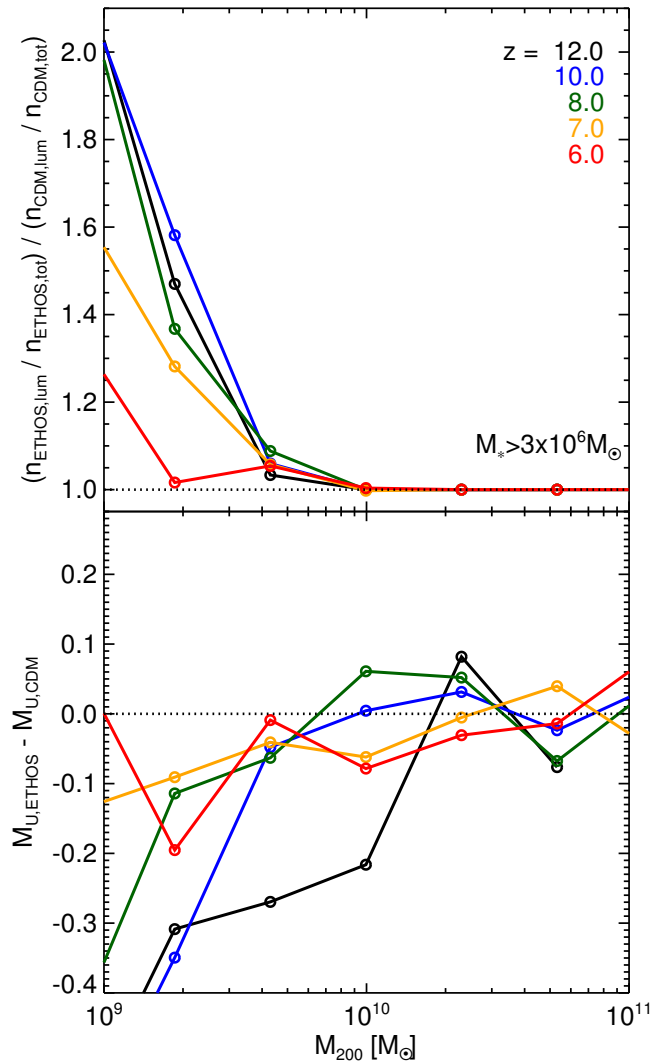


**Figure 4.** Upper panel: Ratio of the fraction of haloes hosting galaxies with  $M_* \geq 3 \times 10^6 M_{\odot}$  in ETHOS to that of CDM as a function of halo mass. Lower panel: Difference in the median  $U$ -band magnitude between ETHOS and CDM as a function of  $M_{200}$ .

affect more strongly other nearby haloes in CDM than in ETHOS seems plausible.

The interplay between the underabundance of low-mass haloes and the delay of the onset of galaxy formation has been studied in the context of WDM, which has a primordial power spectrum cut-off similar to the one in ETHOS. Bose et al. (2016, 2017) showed that, when implementing their semi-analytic model of galaxy formation in a WDM cosmology, galaxy formation is indeed delayed, but the first galaxies that form in WDM are more massive and more gas rich than their CDM counterparts at a fixed halo mass. This results in brighter starbursts, i.e., high star formation rates, as these galaxies form. Therefore, at high redshift, the formation of bright starbursts is more efficient in WDM than in CDM, which also leads to a larger number of ionizing UV photons in WDM compared to CDM. The interplay between these two effects depends on the details of the galaxy formation model and the scale where the primordial cut-off of the power spectrum hap-



pens. Under certain conditions, the enhancement of earlier bright starbursts might be efficient enough to produce a UV luminosity function with a higher amplitude in WDM than in CDM, as it was found in Bose et al. (2017) for a wide range of UV luminosities for  $z > 5$ . The difference in that case was stronger at higher redshifts across all masses, while at a fixed redshift, the difference was larger for more luminous galaxies. For the faintest galaxies the trend was actually reversed, with the amplitude being higher in CDM (e.g., at  $z = 7$ , this reversal happens at  $M_{AB}(UV) \sim -12$ ; see Fig. 12 of Bose et al. 2017). On the other hand, Bose et al. (2016) explored WDM models similar to those in Bose et al. (2017) but with a different supernova feedback implementation (seemingly more consistent with lower mass galaxies at  $z \sim 0$ ) and found that the UV luminosity function in WDM is always below the CDM case (see Fig. 6 of Bose et al. 2016).

### 3.1.2 Impact on galaxy luminosity functions

We investigate the interplay between these competing effects in our simulations. We start by computing the median  $U$ -band luminosities at each halo mass and plot the difference in the median between ETHOS and CDM as a function of  $M_{200}$  in the lower panel of Fig. 4. For all redshift-halo-mass combinations at which we have good statistics, there is a clear preference for ETHOS galaxies to be brighter than CDM ones for host haloes with masses  $< 10^{10} M_{\odot}$ . In this respect, our results are qualitatively similar to those in Bose et al. (2016, 2017).

There are interesting features in the behaviour with redshift of the competing scales that set the galaxy formation threshold. Baryonic physics (mainly heating from reionization) suppresses galaxy formation for halo masses below  $10^{10} M_{\odot}$ <sup>2</sup>, with this mass threshold increasing at lower redshifts as reionization feedback inhibits star formation in progressively larger objects at increasingly lower redshifts (see e.g. Okamoto et al. 2008; Sawala et al. 2016a). This hierarchy is inverted when comparing the suppression (driven by new dark matter physics) of ETHOS haloes relative to CDM haloes where the mass threshold for suppressing halo formation becomes smaller with decreasing redshift. This can be understood as the transfer of power from large to small scales, which causes the evolution of the power spectrum to ‘catch up’ with CDM (clearly reflected in the halo mass function in Fig. 3).

We have found that the two mass scales where galaxy formation is suppressed by either dark or baryonic physics are quite similar:  $M_{200} \approx 10^{10} M_{\odot}$ . This coincidence is driven by the arbitrary choice of stellar mass threshold used to define the luminous fraction ( $M_{*} = 3 \times 10^6 M_{\odot}$ ), but it nevertheless illustrates a relevant point: if a downward change in the slope of the luminosity function were to be detected towards low luminosities, distinguishing it from a primordial cut-off in the power spectrum would be challenging. By contrast, the inverted behaviour of the mass threshold for galaxy formation with redshift resulting from dark and baryonic causes is a promising signature to look for in upcoming observations. Ultimately, this is a first order analysis, a more detailed examination of this process from the theoretical perspective will require significantly higher numerical resolution to map the cut-off in detail ( $\sim 6 \times 10^4 M_{\odot}$  in dark matter particle mass to resolve haloes near the cut-off with  $\sim 100$  particles), an in-depth exploration of the

<sup>2</sup> Strictly, for our purposes, this mass scale is defined as the halo mass where the luminous fraction of haloes (i.e. those having galaxies with  $M_{*} \geq 3 \times 10^6 M_{\odot}$ ), starts to be less than 1.

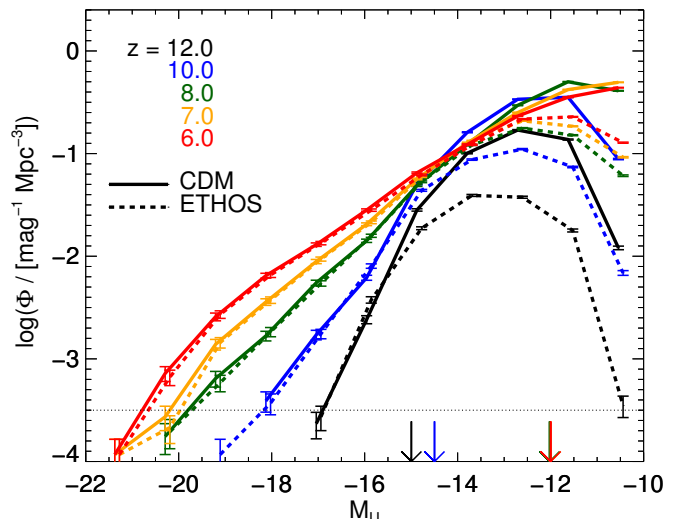


**Figure 5.** The  $U$ -band luminosity functions for CDM (solid curves) and ETHOS (dashed curves). Colours are for different redshifts  $z = 12, 10, 8, 7$  and  $6$  for black, blue, green, orange, and red respectively. The horizontal dotted line marks the galaxy abundance below which low number statistics in the simulation affect the results in a relevant way ( $< 16$  galaxies per bin). The coloured arrows in the horizontal axis mark the approximate magnitude at each redshift below which a fraction of galaxies (approximately 16%, i.e. the fraction below the lower  $1\sigma$  region of the distribution of galaxies in the  $M_{200} - M_U$  plane) are hosted by  $10^8 M_{\odot}$  haloes, and therefore the luminosity functions are at least partially suppressed by mass resolution.

synergy between a primordial cut-off in the power spectrum, and different implementations of the physics responsible for reionization, ideally through direct radiative transfer calculations.

The rate of ionizing photon production is ultimately a convolution of the halo mass function with the UV luminosity per halo mass. The suppression in the ETHOS halo mass function will lead to a lower number of galaxies in total compared to CDM, but the higher luminosity per halo may perceptibly lead to an enhancement in the relative number of bright galaxies, for some threshold in luminosity. To check to what degree either of these is the case, in Fig. 5 we plot the  $U$ -band luminosity functions for our two models at five redshifts in the range  $[12, 6]$ .

At all redshifts, the most marginally resolved galaxies are suppressed in ETHOS relative to CDM with a gap that closes for lower redshifts. There is no redshift at which the abundance of bright ETHOS galaxies exceeds (in a statistically significant way) that of CDM, therefore the enhanced  $U$ -band luminosities of ETHOS galaxies succeeds only in diminishing the intrinsic difference between the ETHOS and CDM halo mass functions. In this regard, and in comparison with WDM, our results are close to those of Bose et al. (2016), and thus, we do not find the overabundance of bright galaxies relative to the CDM case as reported in Bose et al. (2017).

The gap between ETHOS and CDM closes almost completely by  $z = 6$ <sup>3</sup>, which implies that the galaxy population builds up more

<sup>3</sup> This is strictly valid at our resolution limit of  $M_U \sim -12$  for  $z > 8$ . We notice that at higher redshifts, the underabundance of low-mass haloes, and thus low-mass galaxies is strong in ETHOS, but at  $M_U \sim -12$ , resolution issues are relevant at higher redshifts (see arrows in the horizontal axis in Fig. 5) and is thus not possible to quantify the effect adequately.

rapidly in the ETHOS model than in CDM (similar to what was found in Bose et al. 2016 for WDM, although Villanueva-Domingo et al. 2018 found a more persistent difference.). This rapid buildup is a generic feature of models with a cut-off in the power spectrum, seemingly irrespective of the details of the galaxy formation model. This points to a promising observational feature to look for in future observations at the low end of the high-redshift luminosity function.

We note that the strong drop off in the abundance of low-luminosity galaxies at the highest redshifts ( $z > 8$ ) in Fig. 5 is driven at least in part by the resolution limit of our simulations. This is an effect caused by galaxies having higher ongoing star formation rates, and thus being brighter (for a given halo mass), at high redshifts. Thus, at a fixed ( $U$ -band) magnitude, the haloes hosting these galaxies have progressively lower masses at larger redshifts. Once the typical halo mass reaches our resolution limit for the halo mass function ( $\sim 10^8 M_\odot$ ), the abundance of haloes, and hence of galaxies of the associated magnitude, starts being artificially suppressed. For  $z \leq 8$ , this is not an issue down to  $M_U = -12$  since the median halo mass at that magnitude is  $\gtrsim 6 \times 10^8 M_\odot$ . The flattening of the  $U$ -band luminosity function towards lower magnitudes at lower redshift is thus a resolved feature in our simulations and is due to the lower star formation efficiency at lower redshift driven by feedback (stellar and ionizing background). For  $z \leq 8$  we are thus confident that the  $U$ -band luminosity function is sufficiently resolved down to  $M_U = -12$ <sup>4</sup>. For  $z > 8$ , the  $U$ -band is progressively more affected by resolution and by  $z = 14$ , it is properly resolved down to  $M_U \sim -15$  only (see arrows in the horizontal axis in Fig. 5). It is possible that this cut-off may be partly physical if there is a minimum luminosity associated with the initial starburst; we will examine this possibility in a future paper.

### 3.1.3 Predictions for JWST

We have demonstrated so far that the galaxy populations in CDM and ETHOS behave differently at high redshifts near the primordial power spectrum cut-off. A key question is then whether such a difference can be detected to distinguish these models observationally. To this end, we compute the luminosity function in our simulations at wavelengths that will be observed by JWST. We do this using the Flexible Stellar Population Synthesis (FSPS) code<sup>5</sup> (Conroy et al. 2009; Conroy & Gunn 2010). For each star particle in a given simulated galaxy, we construct a simple stellar population (SSP) using as input the metallicity and age of the star particle, and using the initial mass function (IMF) used in our simulation setting (Chabrier IMF; Chabrier 2003); the code then outputs the spectra of the SSP for the particle. A mass-weighted sum is then performed across all particles in the galaxy to compute its spectral energy distribution and total luminosity in the desired band. We compute the FUV and Near Infrared (NIR) luminosity functions, at 150 nm and 1.15  $\mu\text{m}$  rest frame wavelengths, top and middle panels of Fig. 6, respectively. We choose these two wavelengths since they are representative of the FUV, which is a good tracer of recent star formation (young stars), and the NIR, which is a better tracer of the older stellar population (more sensitive to the prior star formation

<sup>4</sup> We note that we have verified, with a lower resolution set of simulations (by a factor of 8 in mass resolution), that the  $U$ -band luminosity function is converged, in the low resolution case, down to the magnitude corresponding to the typical halo mass where the halo mass function is converged.

<sup>5</sup> <https://github.com/cconroy20/fps>

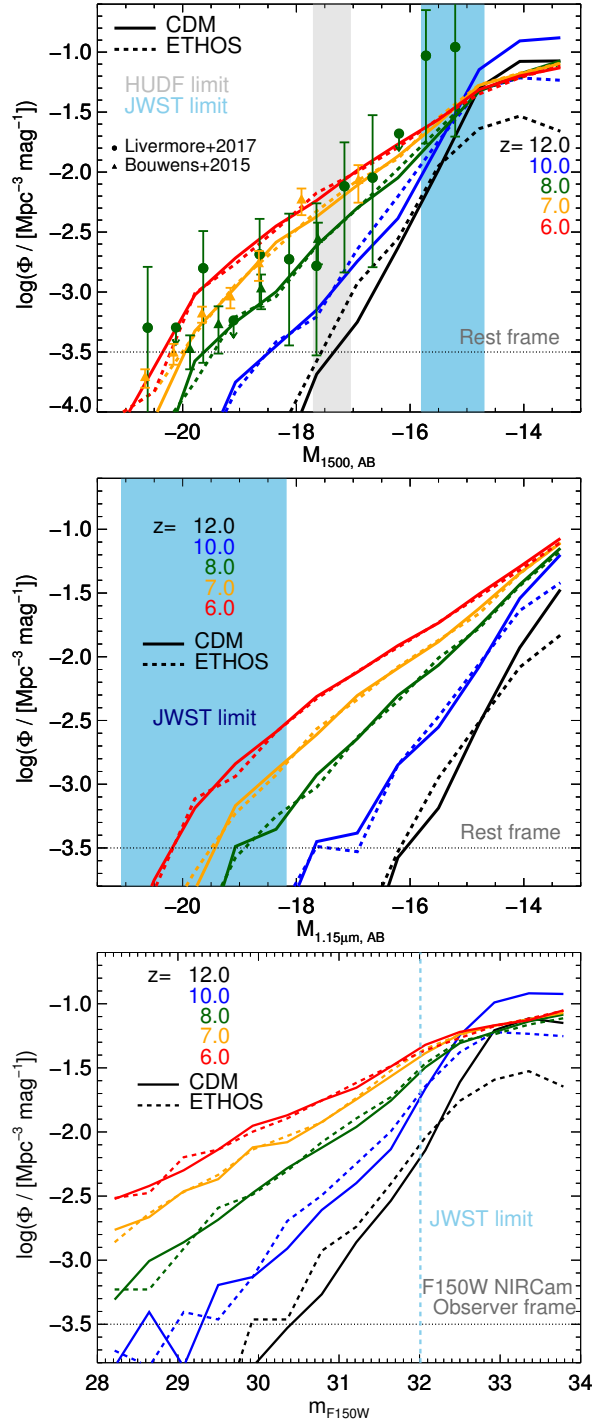


**Figure 6.** FUV (150 nm) and NIR (1.15  $\mu\text{m}$ ) rest-frame luminosity functions, on the top and middle panels, respectively, plus the luminosity function in the observer-frame (using apparent magnitudes) in the JWST F150W band in the bottom panel. The different colours are for different redshifts according to the legend, and the solid and dashed lines are for the CDM and ETHOS cases, respectively. The horizontal dotted line marks the galaxy abundance below which low number statistics in the simulation affect the results in a relevant way ( $< 16$  galaxies per bin). For the upper panel a collection of observations is also shown (Bouwens et al. 2015a; Livermore et al. 2017). The grey (top panel) and blue (top and middle panels) bands are estimated observational limits from HUDF and for an optimistic deep survey with JWST. Interestingly, the differences between ETHOS and CDM start just to be observable at the limit of JWST. In the bottom panel we show the expected JWST magnitude limit in the observer-frame for the F150W NIRCcam filter.



history). In the bottom panel of Fig. 5 we also present the evolution of the luminosity function (in the observer frame) as it would be observed by the Near InfraRed Camera (NIRCam) on JWST (filter F150W), taking into account the transmittance of the NIRCam Filter in JWST<sup>6</sup>.

The luminosity functions in Fig. 6 are shown in monochromatic AB magnitudes, rest-frame in the upper and middle panel, observer-frame in the bottom panel. The FUV (150 nm) luminosity function is shown in the upper panel of Fig. 6. The grey vertical band is roughly the current limit from HST observations (HUDF and CANDELS, see e.g. Bouwens et al. 2015a<sup>7</sup>), while the blue band is the estimated limit for JWST, which is based on the sensitivities for the NIRCam for point source detection with a signal to noise ratio ( $S/N$ ) of 10 and  $10^4$  s exposure<sup>8</sup>. We scaled these sensitivities for the fairly optimistic scenario of a deep field survey with  $10^6$  s exposure (assuming a  $t^{-2}$  scaling), a factor of a few better than the HUDF, and lowering the threshold for point source detection to  $S/N = 5$ . The limit is shown as a band, since the flux sensitivities in Jy are transformed into redshift-dependent sensitivities in the rest-frame magnitudes. We observe that it is approximately at the limit of what JWST can observe in the FUV where the difference between CDM and ETHOS starts to be apparent. Unless the actual final survey strategy and depth for JWST is improved, it will be difficult to distinguish the models in this way, albeit the high-redshift range  $z = 10 - 12$  might be promising.

The rest-frame NIR ( $1.15\mu\text{m}$ ) luminosity function for our simulations is shown in the middle panel of Fig. 6. Since this wavelength is more sensitive to the older stellar population, and hence to the star formation history, it becomes less sensitive, particularly at higher redshifts, to the enhanced starburst phenomena in ETHOS discussed earlier, which mostly affect the recent star formation in the galaxy. The rapid build-up of the galaxy population at the faint-end observed in the FUV is thus not as apparent in the NIR. The difference between the ETHOS and CDM models is however, not apparent until  $z \geq 8$  for  $M_{\text{AB}}(1.15\mu\text{m}) = -14.5$ .

The sensitivity of JWST to NIR wavelengths relies on a different instrument, the Mid InfraRed Instrument (MIRI), which is considerably less sensitive than NIRCam. With a similar optimistic survey scenario as the one described above, we show the sensitivity limit of JWST for the NIR( $1.15\mu\text{m}$ )<sup>9</sup> in the middle panel of Fig. 6. The prospects of JWST reaching the desired magnitudes in NIR are thus extremely low.

A promising strategy is to use gravitational lensing to reach fainter magnitudes. Using data from the Hubble Frontier Fields program, it has been possible to detect very faint galaxies strongly lensed by galaxy clusters. This development makes it possible to probe the UV luminosity function to very faint magnitudes (Livermore et al. 2017; Ishigaki et al. 2018), close to  $M_{\text{UV}} \sim -15$  between  $z = 7 - 9$ . At these magnitudes and redshifts, the 68 per cent confidence interval has an amplitude of  $\sim 1$  dex, which is a factor

of  $\gtrsim 10$  too large compared to the differences between CDM and the benchmark ETHOS models<sup>10</sup>. As a reference, the observations from Livermore et al. (2017) at  $z = 8$  have been added to the upper panel of Fig. 6. With upcoming surveys with the JWST, the prospects of exploiting lensing magnification in a similar way to constrain a primordial cut-off in the power spectrum are promising when combined with a good understanding of the physics of galaxy formation. Although challenging, we think that this might lead to powerful high-redshift constraints for alternative dark matter models in the near future.

### 3.2 Impact on reionization

Above we have studied the differences in the abundance of galaxies in ETHOS and CDM, and pointed out that these differences are not detectable with existing instruments, but could potentially be revealed by upcoming telescopes like JWST. However, we can use the predicted galaxy populations in both models to estimate the optical depth for reionization in CDM and ETHOS. This can potentially constrain or rule out certain non-CDM models, and the question we want to tackle here is whether our benchmark ETHOS model is consistent with current measurements of the reionization history encoded in the optical depth observations. We demonstrate that this is indeed the case.

As mentioned earlier, our simulations do not have radiative transfer and the UV background used in them is not coupled to the actual star formation. Because of this, our approach is based on estimating the fraction of gas that would be ionised in the IGM due to star formation in the simulated galactic population. In particular, we use the predicted star formation rate (SFR) density,  $\rho_{\text{sfr}}$ , to determine the overall production rate of ionizing photons. We thus need to ascertain this quantity as a function of redshift, taking into account the fact that, in CDM at least, it is the faintest, and thus most numerous, galaxies that generate the bulk of the re-ionizing photons.

These faint galaxies are constrained to inhabit haloes that are sufficiently massive for gas to cool to high enough densities to form stars. We take this limit to be given by the virial temperature of the halo at which primordial gas can cool via atomic transitions:  $T_{\text{vir}} = 10^4$  K. The corresponding mass limit is in the range  $5 \times 10^7 - 1.6 \times 10^8 M_{\odot}$ , in the range  $6 \leq z \leq 14$ , with higher mass thresholds for lower redshift. This limit is tantalisingly close to the mass resolution of our simulations. Even though these low mass haloes have poor resolution in star particles (or even are devoid of star particles), the imposed star formation equation of state enables us to calculate the expected SFR given the gas content in a halo, independent of whether this halo contains any star particles. Therefore, whereas other studies have relied on recipes to calculate the UV luminosity of galaxies, we are able to relax many of the assumptions involved in this process by using the SFR in a halo given directly from the simulation data. We thus plot the cumulative SFR as a function of halo mass,  $M_{\text{h}}$ , in Fig. 7, where our definition of halo mass is here the gravitationally bound mass ascribed by the SUBFIND algorithm in order to include subhaloes as well as host haloes. We also include an extrapolation between the spurious-halo resolution threshold  $10^8 M_{\odot}$  and our computed cooling limit for

<sup>6</sup> <https://jwst-docs.stsci.edu/display/JTI/NIRCam+Filters>

<sup>7</sup> The Bouwens et al. (2015a) results were measured at 160 nm rather than 150 nm; we expect that this difference does not affect our conclusions.

<sup>8</sup> The F115W, F150W and F200W are the NIRCam filters sensitive to the rest-frame FUV (150nm) luminosity function in the redshifts shown in the top panel of Fig. 6. Their sensitivities were taken from <https://jwst.stsci.edu/instrumentation/nircam>

<sup>9</sup> The F770W, F1000W, F1130W and F1280W are the MIRI filters sensitive to the rest-frame NIR ( $1.15\mu\text{m}$ ) luminosity function in the redshifts shown in the middle panel of Fig. 6. Their sensitivities are taken from: <https://jwst.stsci.edu/instrumentation/miri>

<sup>10</sup> Notice that increasing the number of cluster lenses would increase the effective volume of the lensing survey and thus would reduce the statistical errors in the reconstructed luminosity function.

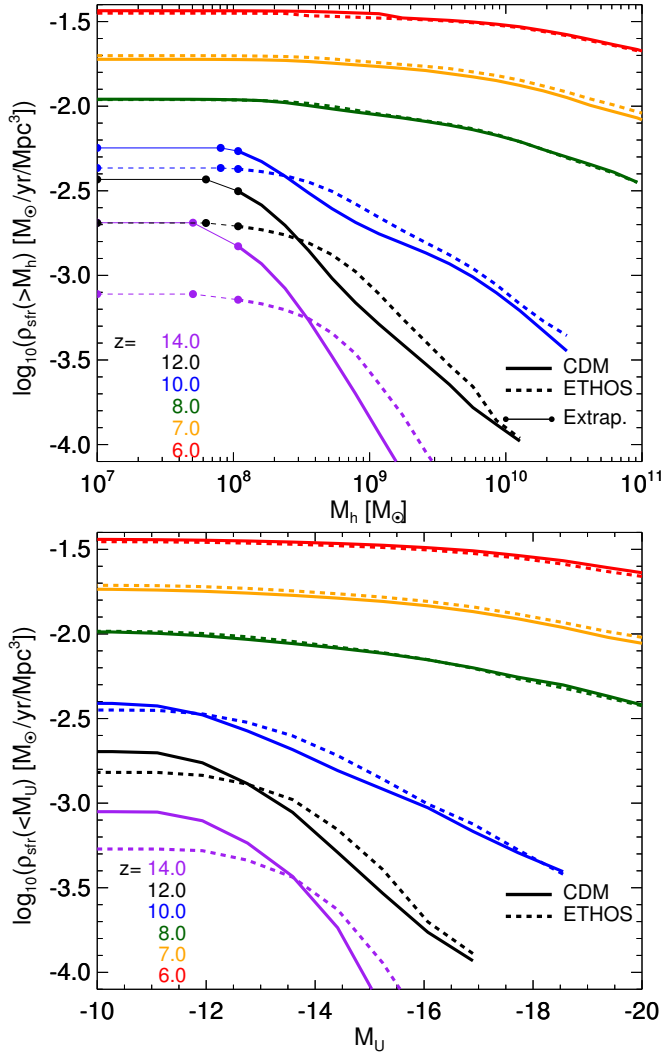


**Figure 7.** Cumulative SFR density as a function of the halo mass,  $M_h$  (top panel) and  $U$ -band luminosity  $M_U$  (bottom panel). Solid (dashed) lines are for CDM (ETHOS). Simulation data is shown as thick lines, extrapolations below  $M_{200} = 10^8 M_\odot$  are shown as thin lines, with the two solid circles (top panel only) bracketing the range where the extrapolation was used. Different colours are for different redshifts according to the legend. Note the addition of the redshift  $z = 14$  (purple) over previous plots.

the halo mass for those redshifts at which the cooling limit is below the resolution limit.

We find that the extrapolation introduces very little extra additional star formation as predicted. The effect of the extrapolation is negligible at low redshift due to the flattening in the  $M_h - \rho_{\text{sfr}}$  relation. The faint slope is shallower in ETHOS, thus the additional star formation introduced by the extrapolation is less than in CDM. CDM clearly produces more stars than ETHOS, despite the enhanced starburst nature of the brighter galaxies in ETHOS.

The behaviour of the cumulative SFR with halo mass is very useful for performing these extrapolations in simulation-based studies, but it cannot be compared directly with observations. We therefore also include in the lower panel of Fig. 7 the cumulative SFR plotted as a function of the  $U$ -band magnitude. The qualitative behaviour of this relation mirrors that of the halo mass counterpart, with brighter ETHOS galaxies exhibiting higher SFRs only for the

contribution of faint CDM galaxies to dominate the total budget. Therefore, the slope of the observed relation is a discriminant between the two models, notwithstanding the difficulties of making these observations as has been shown in the previous section. Note also that, at  $z > 10$ , the total SFR as measured using  $M_h$  is significantly higher than from the  $U$ -band plot. This is a resolution effect, since in the former case we can measure the SFR from the gas in  $< 10^9 M_\odot$  haloes that host no star particles, and therefore do not have a measured  $M_U$ ; this contribution would therefore be missed if we were to use  $M_U$  for our measurement.

We have thus far assumed that all star formation occurs inside collapsed haloes, as these are the only regions in which gas cooling is efficient. However, it is possible that some gas cells in the simulation are not assigned accurately to haloes due to limited resolution, particularly when the host halo is still undergoing its initial collapse. Second, star formation could occur sporadically in uncollapsed regions, which could potentially be relevant for the global SFR before resolved haloes have had an opportunity to collapse. Finally, in the ETHOS model there is also a physical case to be made that some star formation will occur outside haloes. It has been shown using very high resolution simulations (dark matter particle mass  $\sim 10^2 M_\odot$ ) that the WDM cosmology generates smooth filaments that can attain gas densities high enough to form stars (Gao & Theuns 2007). Since ETHOS models behave similarly to WDM, they may exhibit the same effect.

To check for the influence of star formation within unbound regions, we compute the total SFR density in all gas particles in our simulated volume,  $\rho_{\text{sfr},T}$ , and the total SFR density in all gas particles that are bound to haloes,  $\rho_{\text{sfr},B}$ ; the difference between the two is the SFR density in unbound regions  $\rho_{\text{sfr},UB}$ . The quantity of interest is the ratio of  $\rho_{\text{sfr},UB}$  to  $\rho_{\text{sfr},T}$ , which is the contribution to SFR that occurs outside haloes.

For CDM, this ratio is 25 per cent at  $z = 20$ , which drops to 4 per cent by  $z = 14$ , holds steady until  $z = 10$ , and then it drops further to 1 per cent at  $z = 6$ . We speculate that the remarkably high fraction at  $z > 14$  is due to numerical resolution, which reduces to a percent level of the total when haloes start to collapse. The ETHOS simulation shows slightly higher unbound fractions for  $z < 10$ , which is likely due in part to the delay in structure formation caused by the power spectrum cut-off. The discrepancy between the two models could also be explained by some combination of a lower total halo-based SFR in ETHOS or by extra SFR in the proposed filament mode, the latter of which could be manifest as an excess of unbound star formation in ETHOS compared to CDM. We have therefore checked the total unbound SFR in both models, and find that CDM obtains the higher unbound SFR at all redshifts, contrary to what we expect if filament star formation were relevant. We conclude that the excess star formation is due to background noise and resolution effects, and that its magnitude is sufficiently small (particularly for  $z < 14$ ) that it does not affect our results.

We can use our measurements and extrapolations of the SFR density to estimate the optical depth using the analytic procedure introduced in Kuhlen & Faucher-Giguère (2012) (see also Schultz et al. 2014; Robertson et al. 2015). The procedure converts an input star formation rate into an ionizing photon rate, which is then used to calculate the optical depth:

$$\tau(z) = c \langle n_H \rangle \sigma_T \int_0^z f_e Q_{\text{HII}}(z') H^{-1}(z') (1 + z')^2 dz', \quad (1)$$

where  $c$  is the speed of light,  $H(z)$  is the Hubble parameter,  $\sigma_T$  is the Thomson cross section,  $\langle n_H \rangle = X \Omega_b \rho_{\text{crit}}$  is the comov-

ing background density of hydrogen with  $X = 0.75$  being the hydrogen mass fraction, and  $\rho_{\text{crit}}$  the critical density. The number of free electrons per hydrogen nucleus is  $f_e = 1 + \eta Y/4X$ , where  $Y = 0.25$  is the helium mass fraction and we consider helium to be singly ionised ( $\eta = 1$ ) at  $z > 4$  and doubly ionised ( $\eta = 2$ ) at lower redshifts. The volume filling fraction of ionised hydrogen  $Q_{\text{HII}}$  is given by the differential equation:

$$\frac{dQ_{\text{HII}}}{dt} = \left( \frac{1}{\langle n_{\text{H}} \rangle} \right) \frac{dn_{\text{ion}}}{dt} - \frac{Q_{\text{HII}}}{t_{\text{rec}}}, \quad (2)$$

where the volume averaged recombination time  $t_{\text{rec}}$  is:

$$t_{\text{rec}} = [C_{\text{HII}} \alpha_B(T_0)(1 + Y/4X)\langle n_{\text{H}} \rangle(1 + z)^3]^{-1} \\ \approx 0.93 \text{ Gyr} \left( \frac{C_{\text{HII}}}{3} \right)^{-1} \left( \frac{T_0}{2 \times 10^4 \text{ K}} \right)^{0.7} \left( \frac{1 + z}{7} \right)^{-3}, \quad (3)$$

where  $\alpha_B(T_0)$  is the case B hydrogen recombination coefficient at  $T_0 = 2 \times 10^4 \text{ K}$ , which takes the value  $1.6 \times 10^{-13} \text{ cm}^3/\text{s}$ , and  $C_{\text{HII}}$  is the effective clumping factor in ionised gas in the diffuse IGM. There is some uncertainty in the value of  $C_{\text{HII}}$  (see e.g. Fig. 5 of Gnedin 2016). Here we have used a constant value of 3, but note that we also tested the redshift dependent parametrization of (Pawlik et al. 2009), and find that it only effects our final value of  $\tau$  at the 3 per cent level. Finally,  $\dot{n}_{\text{ion}} \equiv dn_{\text{ion}}/dt$  is the globally averaged rate of production of hydrogen ionizing photons:

$$\dot{n}_{\text{ion}} = f_{\text{esc}} \xi_{\text{ion}} \rho_{\text{sfr}}, \quad (4)$$

where  $f_{\text{esc}}$  is an effective fraction of photons produced by the stellar population that escape to ionise the IGM,  $\xi_{\text{ion}}$  is the ionizing photon production efficiency per unit time per unit SFR for a typical stellar population and takes the value  $\log \xi_{\text{ion}} = 53.14$  where  $\xi_{\text{ion}}$  is measured in units of photons  $\text{s}^{-1}/(\text{M}_{\odot}\text{yr}^{-1})$  (Robertson et al. 2015). Note that the relation between  $\dot{n}_{\text{ion}}$  and  $\rho_{\text{sfr}}$  has a degeneracy between  $\xi_{\text{ion}}$  and  $f_{\text{esc}}$ . Therefore, although we focus below in a range of plausible values for  $f_{\text{esc}}$ , this range should be interpreted keeping in mind the degeneracy with  $\xi_{\text{ion}}$ .

We take the SFR density directly from the simulations (with the extrapolation shown in Fig. 7) as opposed to e.g. Robertson et al. (2015), who derived it from a maximum likelihood fit to observations. To maximise the effect of reionization, we adopt a fraction of ionizing photons,  $f_{\text{esc}}$ , that can escape their host haloes into the intergalactic medium, equal to  $f_{\text{esc}} = 0.5$  (as supported by e.g. Fontanot et al. 2014, but see also Wise et al. 2014; Ma et al. 2015, for some discussion of why a lower value may be preferred). In order to calculate the escape fraction in a self-consistent way, we would need to either perform simulations with radiative transfer (e.g. Xu et al. 2016; Gnedin 2016), or post-process our snapshots using a hybrid approach (Ma et al. 2015; Sharma et al. 2016). In general, the value of  $f_{\text{esc}}$  varies greatly temporally and across spatial regions. In the approach we are using, the relevant quantity is an effective redshift-dependent volume-average value of  $f_{\text{esc}}$ . For CDM, Gnedin (2016) computes this value showing that it has a complex behaviour with redshift with a value  $\sim 0.2$  at  $z = 7 - 9$ , and a scatter of a factor of a few depending on the clumping factor of the ionised gas. This value is sensitive to the details of the baryonic physics implementation, and more importantly, it would be different for ETHOS. For the purpose of this paper, we choose a constant value  $f_{\text{esc}}$ , noting that is a relevant source of uncertainty in computing the optical depth. We present the resulting optical depth and its redshift behaviour in Fig. 8.

In our maximal model, the value of  $\tau(z = 15)$  measured for ETHOS is only 8 per cent lower than that of CDM. Both models are

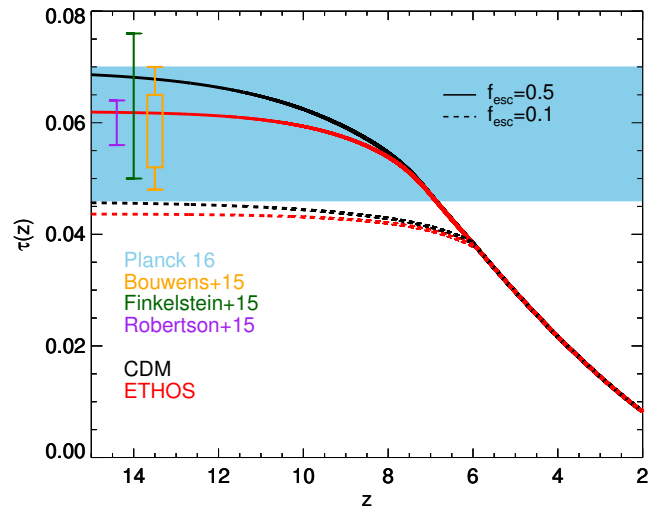


**Figure 8.** Optical depth,  $\tau(z)$  as a function of redshift. Black denotes CDM and red ETHOS. We show calculations in which  $f_{\text{esc}} = 0.5$  (solid lines), and  $f_{\text{esc}} = 0.1$  (dashed lines). The light blue region signifies the allowed region measured in Planck Collaboration et al. (2016b). The orange data point marks the 68 per cent (box) and 95 per cent (error bars) confidence regions from Bouwens et al. (2015b). The purple error bar shows the 68 per cent confidence region measured by Robertson et al. (2015), while the green error bar is likewise the 68 per cent region of Finkelstein et al. (2015).

in good agreement with the constraints derived by Planck. We also compare our results to the estimate of  $\tau$  calculated from the high-redshift luminosity function by Bouwens et al. (2015b), Robertson et al. (2015) and Finkelstein et al. (2015). Both CDM and ETHOS are consistent with these observations.

Setting the escape fraction to 0.1 (dashed lines) reduces the value of  $\tau$  for CDM (ETHOS) by 31 per cent (43 per cent). We also consider a minimal scenario in which ETHOS achieves the lower limit of the Planck measurement without any extrapolation in the SFR density, and find that we require  $f_{\text{esc}} \geq 0.14$  (not plotted). Overall, we conclude that both CDM and ETHOS are essentially consistent with constraints on the optical depth across values of  $f_{\text{esc}}$  from  $\sim 0.1$  to 0.5, with the latter preferring slightly higher  $f_{\text{esc}}$ . We also note that the value of  $f_{\text{esc}}$  is likely to be different between the two models. For instance, it is suggested in Dayal et al. (2017) that a steeper redshift evolution of the ionizing photon escape fraction in WDM models is a way to compensate for the cut-off in the power spectrum. The recombination rate may also be different due to absorption from minihaloes ( $10^4 - 10^7 \text{ M}_{\odot}$ ), which are present in CDM but erased in ETHOS (Yue & Chen 2012; Rudakovskiy & Iakubovskiy 2016). There will be additional uncertainty on our results given the systematic uncertainties on the baryonic physics sub-resolution model, as also argued by Villanueva-Domingo et al. (2018).

Keeping all these caveats/uncertainties in mind, our results indicate that the ETHOS benchmark model, which was calibrated to alleviate the CDM small-scale challenges using dark-matter-only simulations in Vogelsberger et al. (2016), is consistent with high-redshift observables under reasonable assumptions about baryonic physics in this mass regime.



#### 4 CONCLUSIONS

The particle properties of dark matter remain a mystery. Hidden dark matter particle interactions are motivated by a plethora of particle physics models where the dark sector possesses a richer phenomenology with several dark matter species and new forces. A promising search for such interactions lies in looking for their dynamical signature in the formation and evolution of galaxies. Particle models with hidden interactions have an astrophysical impact if they can either (i) alter the primordial linear power spectrum (e.g., through a Silk-like damping caused by dark matter interaction with relativistic particles in the early Universe; e.g. [Böhm et al. 2002](#); [Buckley et al. 2014](#); [Böhm et al. 2014](#)), or (ii) modify the dark matter phase space density in the centre of galactic-size haloes (e.g., through strong dark matter self-interactions; e.g. [Spergel & Steinhardt 2000](#); [Vogelsberger et al. 2012](#); [Rocha et al. 2013](#); [Zavala et al. 2013](#)). These possibilities are central to a recently proposed framework that generalises the theory of structure formation by self-consistently mapping the parameters of allowed particle physics models into effective parameters for structure formation (ETHOS, [Cyr-Racine et al. 2016](#); [Vogelsberger et al. 2016](#)). The ETHOS framework is a powerful way to explore the consequences of new dark matter physics for galaxy formation/evolution. For instance in [Vogelsberger et al. \(2016\)](#), dark matter-only simulations were used to find a benchmark model (ETHOS-4, which we refer to as ETHOS in this paper for simplicity) that eases the tensions with some of the outstanding small-scale challenges facing the standard CDM model in regards to the properties of Milky Way satellites, i.e., their abundance and inferred inner dark matter structure (for a review see [Bullock & Boylan-Kolchin 2017](#)).

In order to further explore and constrain the ETHOS framework, we have studied here the consequences of this specific ETHOS benchmark model in the high redshift Universe, which is an environment very different from that of the Milky Way. Our goal was to understand the consistency of the model with high-redshift observations. To accomplish this, we have performed cosmological hydrodynamical simulations with a well-developed galaxy formation model. The simulations cover a volume of  $(36.2 \text{ Mpc})^3$ , and each run employs a simulation dark matter particle mass of  $1.76 \times 10^6 M_\odot$  and dark matter softening length of 724 pc. The average gas cell mass is  $2.69 \times 10^5 M_\odot$  and the gas softening length is adaptive with a minimum of 181 pc. This mass resolution is comparable to the highest numerical resolution of any resolved uniform volume hydrodynamical simulations of an alternative dark matter model.

At high redshifts ( $z \geq 6$ ), the main differences between the benchmark ETHOS model and the standard CDM model are caused by the former having a primordial cut-off in the power spectrum due to dark matter-dark radiation interactions, suppressed for wavenumbers  $\gtrsim 14.5 \text{ Mpc}^{-1}$ , with an oscillating amplitude at higher wavenumbers (see Fig. 1). This cut-off reduces the number density of low mass haloes and also delays the onset of structure formation across the mass hierarchy. These two phenomena lead to a suppression of galaxy formation at low masses, and thus to a reduction of the available ionizing photons responsible of reionizing the Universe. Both of these are connected to the observed low-luminosity end of the UV luminosity function (e.g. [Bouwens et al. 2015a](#); [Livermore et al. 2017](#); [Ishigaki et al. 2018](#)), and the optical depth of cosmic microwave background photons, denoted by  $\tau$  ([Planck Collaboration et al. 2016b](#)).

We find that although the number of low mass galaxies is suppressed in ETHOS relative to CDM, the difference is still indistin-

guishable in current observations:  $\sim 0.1$  dex for  $M_U \sim -14.5$  at  $z \sim 8$  in the FUV luminosity function, while the observational errors ( $1\sigma$ ) at similar redshifts and slightly brighter magnitudes are  $\sim 1$  dex based on [Livermore et al. 2017](#); [Ishigaki et al. 2018](#) (see upper panel of Fig. 6). This leaves the prospects of progressively differentiating these models in this way to upcoming galaxy surveys, beginning with those planned for the JWST. Based on our simulations, we have presented predictions for the rest-frame FUV (1500 nm) and NIR ( $1.15 \mu\text{m}$ ) luminosity functions, as well as in the observer-frame for one of the filters (F150W) of the NIRCам instrument in JWST (Fig. 6). Predictions for other filters are available upon request to the authors.

On the other hand, we also find that, for the mass range affected by the primordial cut-off of the power spectrum, high-redshift galaxies in ETHOS are brighter per unit halo mass than is the case for CDM (see Fig. 4), a result that is consistent overall with recent studies based on a WDM cosmology coupled with semi-analytic model of galaxy formation ([Bose et al. 2017, 2016](#)). Since these results are based on very different models of galaxy formation and evolution, it suggests that having high-redshift low-mass galaxies with a higher efficiency of star formation is a generic feature of models with a cut-off in the primordial power spectrum.

The brighter starbursts in ETHOS partially compensate for the deficit of UV photons due to the low galaxy number density. This compensating effect reduces the naive expectations of the impact of the cut-off in the power spectrum in the optical depth  $\tau(z)$ . To estimate the optical depth from our simulations, we use the SFR measured directly from the gas properties in our simulations to compute the cumulative SFR density down to halo masses of  $10^8 M_\odot$ , which is our effective resolution limit in the halo mass function. By this halo mass, the SFR density has essentially converged to a maximum value which we use to estimate analytically the number density of ionizing photons and thus the optical depth. We find that the bright ETHOS starburst galaxies provide a boost to the optical depth at all  $z > 6$  over the naive expectations. Ultimately however, the great number density of small galaxies in CDM wins out over the relative brightness of their ETHOS counterparts, such that the total ETHOS optical depth is still suppressed relative to CDM, but only by  $\lesssim 10$  per cent within a range of values of the escape fraction in between 0.1 and 0.5 (see Fig. 8). This suppression is relatively small compared to the uncertainties in both the experimentally measured optical depth of the CMB, the UV-photon escape fraction, and the ionizing photon production rate efficiency. Within the assumptions of our method, we find that the CDM and ETHOS models are equally consistent with current observations. A significant improvement upon our results can only be achieved by a self-consistent calculation of the escape fraction in the ETHOS and CDM simulations; i.e., including radiative transfer that accounts for clumping and self-shielding, and a better understanding of the impact of galaxy formation modelling in the faint end of the luminosity function at very high redshifts.

We conclude that the ETHOS benchmark model, chosen to alleviate the small-scale issues of CDM at the scale of satellite galaxies, is currently consistent with the high-redshift abundance of galaxies, and with reionization constraints. Limitations of this study include our baryonic mass resolution ( $\sim 2 \times 10^5 M_\odot$  average mass cell), which is still too coarse to resolve the  $U$ -band luminosity function down to the faintest galaxies responsible from reionization (particularly at  $z > 8$ ). This adds uncertainty in our calculation of the global SFR density, which in this work is based on the SFR calculated in resolved haloes based on their gas content, but that lack the resolution to form the galaxies within. We have also not

explored variations over the particular baryonic physics implementation we have used. Studying the synergy between variations of the dark and baryonic physics (i.e. varying the effective parameters in the dark matter and baryonic physics sectors that impact galaxy formation and evolution) is one of our near future plans. Finally, self-consistent radiation-hydrodynamics simulations (Kannan et al. in prep) are needed to explore in more detail the reionization history and to make detailed predictions of the high-redshift galaxy population for CDM and non-CDM models.

## ACKNOWLEDGEMENTS

We thank Torsten Bringmann, Rachael Livermore, Steve Finkelstein and Christina Williams for useful comments and suggestions. We further thank Volker Springel for giving us access to AREPO, and Jose Oñorbe for help with computing the optical depth. MRL is supported by a COFUND/Durham Junior Research Fellowship under EU grant 609412. MRL and JZ acknowledge support by a Grant of Excellence from the Icelandic Research Fund (grant number 173929–051). MV acknowledges support through an MIT RSC award, the support of the Alfred P. Sloan Foundation, and support by NASA ATP grant NNX17AG29G. MBK acknowledges support from NSF grant AST-1517226 and from NASA grants NNX17AG29G and HST-AR-13888, HST-AR-13896, HST-AR-14282, and HST-AR-14554 from the Space Telescope Science Institute, which is operated by AURA, Inc., under NASA contract NAS5-26555. F.-Y. C.-R. acknowledges the support of the National Aeronautical and Space Administration ATP grant NNX16AII2G at Harvard University. Some numerical calculations were run on using allocation TG-AST140080 granted by the Extreme Science and Engineering Discovery Environment (XSEDE), which is supported by the NSF.

## REFERENCES

- Bertschinger E., 2006, *Phys. Rev. D*, **74**, 063509
- Blumenthal G. R., Faber S. M., Primack J. R., Rees M. J., 1984, *Nature*, **311**, 517
- Bode P., Ostriker J. P., Turok N., 2001, *ApJ*, **556**, 93
- Boehm C., Riazuelo A., Hansen S. H., Schaeffer R., 2002, *Phys. Rev. D*, **66**, 083505
- Boehm C., Schewtschenko J. A., Wilkinson R. J., Baugh C. M., Pascoli S., 2014, *MNRAS*, **445**, L31
- Bose S., Frenk C. S., Hou J., Lacey C. G., Lovell M. R., 2016, *MNRAS*, **463**, 3848
- Bose S., et al., 2017, *MNRAS*, **464**, 4520
- Bouwens R. J., et al., 2015a, *ApJ*, **803**, 34
- Bouwens R. J., Illingworth G. D., Oesch P. A., Caruana J., Holwerda B., Smit R., Wilkins S., 2015b, *ApJ*, **811**, 140
- Boyarsky A., Ruchayskiy O., Iakubovskiy D., Franse J., 2014, *Physical Review Letters*, **113**, 251301
- Boylan-Kolchin M., Bullock J. S., Kaplinghat M., 2011, *MNRAS*, **415**, L40
- Bozek B., Boylan-Kolchin M., Horiuchi S., Garrison-Kimmel S., Abazajian K., Bullock J. S., 2016, *MNRAS*, **459**, 1489
- Brinckmann T., Zavala J., Rapetti D., Hansen S. H., Vogelsberger M., 2018, *MNRAS*, **474**, 746
- Bringmann T., Hofmann S., 2007, *J. Cosmology Astropart. Phys.*, **4**, 016
- Buckley M. R., Zavala J., Cyr-Racine F.-Y., Sigurdson K., Vogelsberger M., 2014, *Phys. Rev. D*, **90**, 043524
- Bulbul E., Markevitch M., Foster A., Smith R. K., Loewenstein M., Randall S. W., 2014, *ApJ*, **789**, 13
- Bullock J. S., Boylan-Kolchin M., 2017, *ARA&A*, **55**, 343
- Chabrier G., 2003, *PASP*, **115**, 763
- Chan T. K., Kereš D., Oñorbe J., Hopkins P. F., Muratov A. L., Faucher-Giguère C.-A., Quataert E., 2015, *MNRAS*, **454**, 2981
- Chen X., Kamionkowski M., Zhang X., 2001, *Phys. Rev. D*, **64**, 021302
- Colín P., Avila-Reese V., Valenzuela O., 2000, *ApJ*, **542**, 622
- Colín P., Avila-Reese V., Valenzuela O., Firmani C., 2002, *ApJ*, **581**, 777
- Conroy C., Gunn J. E., 2010, *ApJ*, **712**, 833
- Conroy C., Gunn J. E., White M., 2009, *ApJ*, **699**, 486
- Crain R. A., et al., 2015, *MNRAS*, **450**, 1937
- Creasey P., Sameie O., Sales L. V., Yu H.-B., Vogelsberger M., Zavala J., 2017, *MNRAS*, **468**, 2283
- Cyr-Racine F.-Y., Sigurdson K., 2013, *Phys. Rev.*, **D87**, 103515
- Cyr-Racine F.-Y., Sigurdson K., Zavala J., Bringmann T., Vogelsberger M., Pfrommer C., 2016, *Phys. Rev. D*, **93**, 123527
- Davé R., Spergel D. N., Steinhardt P. J., Wandelt B. D., 2001, *ApJ*, **547**, 574
- Dayal P., Choudhury T. R., Bromm V., Pacucci F., 2017, *ApJ*, **836**, 16
- Di Cintio A., Brook C. B., Macciò A. V., Stinson G. S., Knebe A., Dutton A. A., Wadsley J., 2014, *MNRAS*, **437**, 415
- Dooley G. A., Peter A. H. G., Vogelsberger M., Zavala J., Frebel A., 2016, *MNRAS*, **461**, 710
- Dubois Y., et al., 2014, *MNRAS*, **444**, 1453
- Elbert O. D., Bullock J. S., Garrison-Kimmel S., Rocha M., Oñorbe J., Peter A. H. G., 2015, *MNRAS*, **453**, 29
- Faucher-Giguère C.-A., Lidz A., Zaldarriaga M., Hernquist L., 2009, *ApJ*, **703**, 1416
- Feng J. L., 2010, *Ann.Rev.Astron.Astrophys.*, **48**, 495
- Feng J. L., Kaplinghat M., Tu H., Yu H.-B., 2009, *J. Cosmology Astropart. Phys.*, **7**, 004
- Finkelstein S. L., et al., 2015, *ApJ*, **810**, 71
- Fitts A., et al., 2017, *MNRAS*, **471**, 3547
- Flores R. A., Primack J. R., 1994, *ApJ*, **427**, L1
- Fontanot F., Cristiani S., Pfrommer C., Cupani G., Vanzella E., 2014, *MNRAS*, **438**, 2097
- Gao L., Theuns T., 2007, *Science*, **317**, 1527
- Garzilli A., Boyarsky A., Ruchayskiy O., 2017, *Physics Letters B*, **773**, 258
- Genel S., et al., 2014, *MNRAS*, **445**, 175
- Gnedin N. Y., 2016, *ApJ*, **825**, L17
- Governato F., et al., 2010, *Nature*, **463**, 203
- Green A. M., Hofmann S., Schwarz D. J., 2004, *MNRAS*, **353**, L23
- Hofmann S., Schwarz D. J., Stöcker H., 2001, *Phys. Rev. D*, **64**, 083507
- Iršič V., et al., 2017, *Phys. Rev. D*, **96**, 023522
- Ishigaki M., Kawamata R., Ouchi M., Oguri M., Shimasaku K., Ono Y., 2018, *ApJ*, **854**, 73
- Kamada A., Kaplinghat M., Pace A. B., Yu H.-B., 2017, *Physical Review Letters*, **119**, 111102
- Kaplinghat M., Tulin S., Yu H.-B., 2016, *Physical Review Letters*, **116**, 041302
- Kennedy R., Frenk C., Cole S., Benson A., 2014, *MNRAS*, **442**, 2487
- Kim S. Y., Peter A. H. G., Hargis J. R., 2017, preprint, ([arXiv:1711.06267](https://arxiv.org/abs/1711.06267))
- Klypin A., Kravtsov A. V., Valenzuela O., Prada F., 1999, *ApJ*, **522**, 82
- Klypin A., Karachentsev I., Makarov D., Nasonova O., 2015, *MNRAS*, **454**, 1798
- Kuhlen M., Faucher-Giguère C.-A., 2012, *MNRAS*, **423**, 862
- Livermore R. C., Finkelstein S. L., Lotz J. M., 2017, *ApJ*, **835**, 113
- Loeb A., Weiner N., 2011, *Physical Review Letters*, **106**, 171302
- Lovell M. R., et al., 2012, *MNRAS*, **420**, 2318
- Lovell M. R., Frenk C. S., Eke V. R., Jenkins A., Gao L., Theuns T., 2014, *MNRAS*, **439**, 300
- Lovell M. R., et al., 2016, *MNRAS*, **461**, 60
- Lovell M. R., et al., 2017, *MNRAS*, **468**, 4285
- Ma X., Kasen D., Hopkins P. F., Faucher-Giguère C.-A., Quataert E., Kereš D., Murray N., 2015, *MNRAS*, **453**, 960
- Moore B., 1994, *Nature*, **370**, 629
- Moore B., Ghigna S., Governato F., Lake G., Quinn T., Stadel J., Tozzi P., 1999, *ApJ*, **524**, L19
- Munshi F., et al., 2013, *ApJ*, **766**, 56
- Murgia R., Merle A., Viel M., Totzauer M., Schneider A., 2017, *J. Cosmology Astropart. Phys.*, **11**, 046

- Naab T., Ostriker J. P., 2017, *ARA&A*, **55**, 59
- Oñorbe J., Boylan-Kolchin M., Bullock J. S., Hopkins P. F., Kereš D., Faucher-Giguère C.-A., Quataert E., Murray N., 2015, *MNRAS*, **454**, 2092
- Okamoto T., Gao L., Theuns T., 2008, *MNRAS*, **390**, 920
- Papastergis E., Martin A. M., Giovanelli R., Haynes M. P., 2011, *ApJ*, **739**, 38
- Pawlik A. H., Schaye J., van Scherpenzeel E., 2009, *MNRAS*, **394**, 1812
- Pillepich A., et al., 2018, *MNRAS*, **473**, 4077
- Planck Collaboration et al., 2014, *A&A*, **571**, A16
- Planck Collaboration et al., 2016a, *A&A*, **594**, A13
- Planck Collaboration et al., 2016b, *A&A*, **596**, A108
- Polisensky E., Ricotti M., 2011, *Phys. Rev. D*, **83**, 043506
- Pontzen A., Governato F., 2012, *MNRAS*, **421**, 3464
- Puchwein E., Pfrommer C., Springel V., Broderick A. E., Chang P., 2012, *MNRAS*, **423**, 149
- Read J. I., Iorio G., Agertz O., Fraternali F., 2017, *MNRAS*, **467**, 2019
- Robertson B. E., Ellis R. S., Furlanetto S. R., Dunlop J. S., 2015, *ApJ*, **802**, L19
- Robles V. H., et al., 2017, *MNRAS*, **472**, 2945
- Rocha M., Peter A. H. G., Bullock J. S., Kaplinghat M., Garrison-Kimmel S., Oñorbe J., Moustakas L. A., 2013, *MNRAS*, **430**, 81
- Rudakovskiy A., Iakubovskiy D., 2016, *J. Cosmology Astropart. Phys.*, **6**, 017
- Sawala T., et al., 2016a, *MNRAS*, **456**, 85
- Sawala T., et al., 2016b, *MNRAS*, **457**, 1931
- Schaye J., et al., 2015, *MNRAS*, **446**, 521
- Schultz C., Oñorbe J., Abazajian K. N., Bullock J. S., 2014, *MNRAS*, **442**, 1597
- Sharma M., Theuns T., Frenk C., Bower R., Crain R., Schaller M., Schaye J., 2016, *MNRAS*, **458**, L94
- Somerville R. S., Davé R., 2015, *ARA&A*, **53**, 51
- Spergel D. N., Steinhardt P. J., 2000, *Physical Review Letters*, **84**, 3760
- Spergel D. N., Flauger R., Hložek R., 2015, *Phys. Rev. D*, **91**, 023518
- Springel V., 2010, *MNRAS*, **401**, 791
- Springel V., et al., 2005, *Nature*, **435**, 629
- Teyssier R., Pontzen A., Dubois Y., Read J. I., 2013, *MNRAS*, **429**, 3068
- Tollet E., et al., 2016, *MNRAS*, **456**, 3542
- Torrey P., Vogelsberger M., Genel S., Sijacki D., Springel V., Hernquist L., 2014, *MNRAS*, **438**, 1985
- Tulin S., Yu H.-B., 2018, *Phys. Rep.*, **730**, 1
- Vegetti S., Vogelsberger M., 2014, *MNRAS*, **442**, 3598
- Viel M., Becker G. D., Bolton J. S., Haehnelt M. G., 2013, *Phys. Rev. D*, **88**, 043502
- Villanueva-Domingo P., Gnedin N. Y., Mena O., 2018, *ApJ*, **852**, 139
- Vogelsberger M., Zavala J., 2013, *MNRAS*, **430**, 1722
- Vogelsberger M., Zavala J., Loeb A., 2012, *MNRAS*, p. 3127
- Vogelsberger M., Genel S., Sijacki D., Torrey P., Springel V., Hernquist L., 2013, *MNRAS*, **436**, 3031
- Vogelsberger M., et al., 2014a, *MNRAS*, **444**, 1518
- Vogelsberger M., Zavala J., Simpson C., Jenkins A., 2014b, *MNRAS*, **444**, 3684
- Vogelsberger M., et al., 2014c, *Nature*, **509**, 177
- Vogelsberger M., Zavala J., Cyr-Racine F.-Y., Pfrommer C., Bringmann T., Sigurdson K., 2016, *MNRAS*, **460**, 1399
- Wang J., White S. D. M., 2007, *MNRAS*, **380**, 93
- Weinberger R., et al., 2017, *MNRAS*, **465**, 3291
- White S. D. M., Rees M. J., 1978, *MNRAS*, **183**, 341
- White S. D. M., Frenk C. S., Davis M., 1983, *ApJ*, **274**, L1
- Wise J. H., Demchenko V. G., Halicek M. T., Norman M. L., Turk M. J., Abel T., Smith B. D., 2014, *MNRAS*, **442**, 2560
- Xu H., Wise J. H., Norman M. L., Ahn K., O’Shea B. W., 2016, *ApJ*, **833**, 84
- Yoshida N., Springel V., White S. D. M., Tormen G., 2000, *ApJ*, **544**, L87
- Yue B., Chen X., 2012, *ApJ*, **747**, 127
- Zavala J., Jing Y. P., Faltenbacher A., Yepes G., Hoffman Y., Gottlöber S., Catinella B., 2009, *ApJ*, **700**, 1779
- Zavala J., Vogelsberger M., Walker M. G., 2013, *MNRAS*, **431**, L20
- Zolotov A., et al., 2012, *ApJ*, **761**, 71
- van den Aarssen L. G., Bringmann T., Pfrommer C., 2012, *Physical Review Letters*, **109**, 231301

This paper has been typeset from a  $\text{\TeX}/\text{\LaTeX}$  file prepared by the author.